

DeepSaliency: Multi-Task Deep Neural Network Model for Salient Object Detection

Xi Li, Liming Zhao, Lina Wei, MingHsuan Yang, Fei Wu, Yuetong Zhuang, Haibin Ling, and Jingdong Wang

Abstract—A key problem in salient object detection is how to effectively model the semantic properties of salient objects in a data-driven manner. In this paper, we propose a multi-task deep saliency model based on a fully convolutional neural network (FCNN) with global input (whole raw images) and global output (whole saliency maps). In principle, the proposed saliency model takes a data-driven strategy for encoding the underlying saliency prior information, and then sets up a multi-task learning scheme for exploring the intrinsic correlations between saliency detection and semantic image segmentation. Through collaborative feature learning from such two correlated tasks, the shared fully convolutional layers produce effective features for object perception. Moreover, it is capable of capturing the semantic information on salient objects across different levels using the fully convolutional layers, which investigates the feature-sharing properties of salient object detection with a great reduction of feature redundancy. Finally, we present a graph Laplacian regularized nonlinear regression model for saliency refinement. Experimental results demonstrate the effectiveness of our approach in comparison with the state-of-the-art approaches.

Index Terms—salient object detection, CNN, multi-task, data-driven.

I. INTRODUCTION

As an important and challenging problem in computer vision, salient object detection [1], [2], [3], [4], [5], [6], [7], [8], [9], [10] aims to automatically discover and locate the visually interesting regions that are consistent with human perception. It has a wide range of applications such as object tracking and recognition, image compression, image and video retrieval, photo collage, video event detection, and so on. The focus of salient object detection is on designing various computational models to measure image saliency, which is useful for segmentation.

From the perspective of human perception, the semantic properties of an image are typically characterized by the objects and their contexts within the same scene. In principle, each object can be represented on three different levels (i.e., low-level, mid-level, and high-level). The low-level visual cues [11], [12] are concerned with primitive image features such as color, edge, and texture. The mid-level features [13], [14] typically correspond to the object information on contour, shape, and spatial context. In comparison, the high-level information is associated with the object recognition, segmentation as well as the intrinsic semantic interactions among objects.

X. Li, L. Zhao, L. Wei, F. Wu and Y. Zhuang are with College of Computer Science, Zhejiang University, Hangzhou, China.

M. Yang is with Electrical Engineering and Computer Science at University of California, Merced, United States.

H. Ling is with Highscene Information Technology Co., Ltd, China.

J. Wang is with Media Computing Group, Microsoft Research Asia, China.

along with background [15], [16], [17], [18]. In essence, the task of salient object detection is related to these three levels at the same time. Therefore, how to effectively model all the above factors in a unified learning framework is a key and challenging issue to solve in salient object detection.

Early approaches in this field typically formulate salient object detection as the problem of image contrast analysis in a center-surround or object-background manner. These approaches detect the salient objects by computing the local center-surround differences [11], [19], [20], or evaluating the region uniqueness and rarity in the scene [21], [22], [23]. Furthermore, a number of approaches heuristically enforce some predefined priors on the process of saliency detection such as image center priors, large-sized closed regions [24], and object semantic meanings [15]. In addition, several approaches [14], [25], [26], [27] attempt to utilize the background prior information to perform the label propagation procedure in a spatial structural graph. However, such prior models have to be carefully tailored for adapting to different types of image data with a wide variety of objects and their contextual interactions, thereby making them less applicable to a wide range of problems in practice. For example, salient objects often appear at the image boundary (far away from the image center), and thus the center prior is less useful. Moreover, as parts of salient objects may be similar to some background regions, it is difficult to detect them based on the contrast information. Motivated by these observations, we need to construct an adaptive model to effectively capture the intrinsic semantic properties of salient objects and their essential differences from the background in a pure data-driven approach. Meanwhile, the model is supposed to encode the saliency information across different levels (from low-level to high-level), as shown in Figure 1. To address these problems, a number of deep learning approaches [28], [29], [30], [31], [32] have emerged as a powerful tool of data-driven multi-granularity image understanding. Therefore, how to design an effective deep learning model for saliency detection is the focus of this work.

Recent data-driven saliency models [33], [34], [16], [35] aim to directly capture the semantic properties of salient objects in terms of supervised learning from a collection of training data with saliency annotations. By independently modelling all local image patches (treated as training samples for classification or regression), these approaches are often incapable of effectively capturing the feature-sharing properties of salient objects, leading to a high feature redundancy and an expensive computational cost. Furthermore, they mainly focus on directly learning a saliency prediction function from the saliency train-

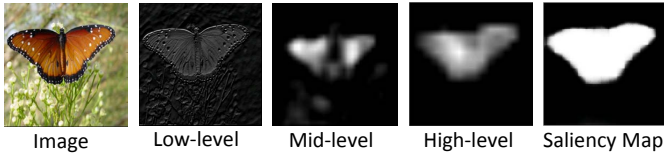


Fig. 1: Illustration of multi-level semantic information obtained by FCNN. FCNN captures the saliency properties across different levels (i.e., low-level (image edge information), mid-level (coarse-grained shape), and high-level (semantic object information)).

ing data, and thus lack the capability of effectively modeling the object perception properties of saliency detection (i.e., objectness). In practice, such object perception properties are very helpful to discovering salient objects.

In this paper, we propose a multi-task deep saliency model based on a fully convolutional neural network (FCNN) with global input (whole raw images) and global output (whole saliency maps). In principle, the deep saliency model takes a data-driven learning pipeline for capturing the underlying saliency prior knowledge, and subsequently builds a multi-task learning scheme for exploring the intrinsic correlations between the tasks of saliency detection and semantic image segmentation, which share the fully convolutional layers in the learning process of FCNN. Through collaborative feature learning from such two correlated tasks, discriminative features are extracted to effectively encode the object perception information. Moreover, the deep saliency model has the capability of capturing the semantic information on salient objects across different levels using FCNN, which explores the feature-sharing properties of salient objects. In addition, we further develop a graph Laplacian regularized nonlinear regression scheme for saliency refinement to generate a fine-grained boundary-preserving saliency map.

The main contributions of this work are summarized as follows:

1) We propose a multi-task FCNN based approach to model the intrinsic semantic properties of salient objects in a totally data-driven manner. The proposed approach performs collaborative feature learning for the two correlated tasks (i.e., saliency detection and semantic image segmentation), which generally leads to the performance improvement of saliency detection in object perception. Moreover, it effectively enhances the feature-sharing capability of salient object detection by using the fully convolutional layers, resulting in a significant reduction of feature redundancy.

2) We present a fine-grained superpixel-driven saliency refinement model based on graph Laplacian regularized nonlinear regression with the output of the proposed FCNN model. The presented model admits a closed-form solution, and is able to accurately preserve object boundary information for saliency detection.

II. PROPOSED APPROACH

A. Overview

The proposed salient object detection approach mainly consists of two components: 1) multi-task fully convolutional neural network (FCNN); and 2) nonlinear regression for saliency refinement. For 1), we perform the task of learning a FCNN

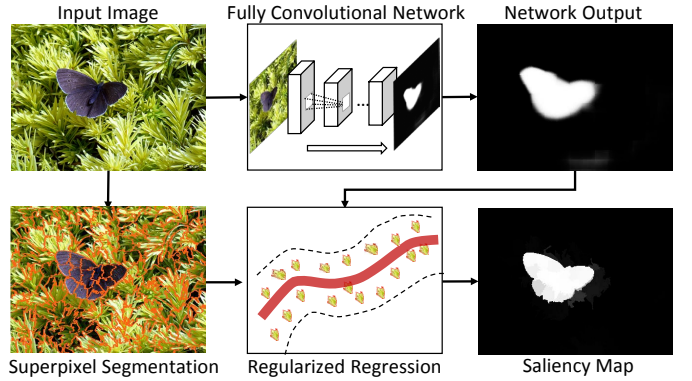


Fig. 2: Illustration of our approach for salient object detection. First, a fully convolutional neural network takes the whole image as input and predicts the saliency map by capturing the semantic information on salient objects across different levels. Second, a Laplacian regularized nonlinear regression scheme based on the superpixel graph is used to produce a fine-grained boundary-preserving saliency map.

saliency model in conjunction with the task of pixelwise object class segmentation. These two tasks share a set of fully convolutional layers for extracting the features of a given image on multiple levels, and meanwhile have different deconvolutional layers that are tailored for different applications, including saliency detection and object class segmentation. Such a multi-task learning scheme enables saliency detection to have a better object perception capability. For 2), based on the output saliency results from FCNN, we further refine the saliency map by graph Laplacian regularized nonlinear regression, thereby generating fine-grained boundary-preserving saliency results. Figure 2 shows the main steps of the proposed salient object detection approach.

B. Multi-Task FCNN

1) *Network Architecture*: As illustrated in Figure 3, our FCNN scheme carries out the task of saliency detection in conjunction with the task of object class segmentation. More specifically, the convolutional layers of our FCNN between the object segmentation and saliency detection tasks are shared.

The shared convolution part aims to extract a collection of features for the input image across different semantic levels. This part processes the input RGB image by a sequence of convolutional operations across 15 convolutional layers, each of which is equipped with a Rectified Linear Unit(ReLU) [36]. In addition, some layers are followed by the max pooling operations, as shown in Figure 3. In practice, the first 13 layers are initialized from the VGG nets [29] (pretrained over the ImageNet dataset [37] with a large number of semantic object classes), resulting in the discriminative power of our shared convolution part for semantic object classification. To further model the spatial correlations of the whole image, we only use the fully convolutional learning architecture (without any fully connected layers). That is because the fully convolutional operations has the capability of sharing the convolutional features across the entire image, leading to the reduction of feature redundancy. Therefore, the fully convolutional learning architecture is simple and efficient with global input and global output.

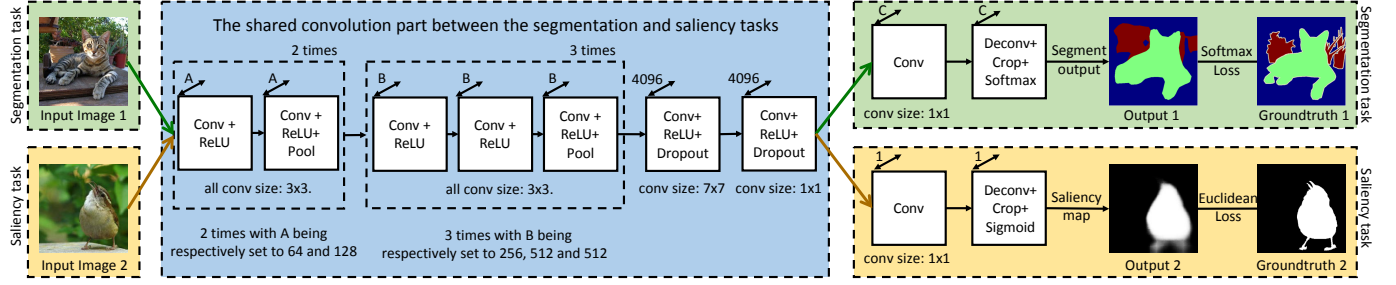


Fig. 3: Architecture of the proposed fully convolutional neural network for training. The FCNN scheme carries out the task of saliency detection in conjunction with the task of object class segmentation, which share a convolution part with 15 layers. The segmentation task seeks for the intrinsic object semantic information of the image, while the saliency task aims to find the salient objects. For the saliency detection task, we only use the saliency-related network for testing.

2) *Object Segmentation Task*: In the segmentation task, features extracted from the shared convolution part are fed into the semantic segmentation task, which seeks for the intrinsic object semantic information for the image. We first apply one layer with 1×1 sized convolution to compute the segmentation score map. To make the output map have the same size as the input image, we need a deconvolution layer, which is also used in the FCN net [32]. The parameters in the deconvolution layer are updated during training to learn an upsampling function. The upsampled outputs are then cropped to the same size of the input image. Thus, the network takes the whole image as input and produces the corresponding pixelwise dense prediction results with the same size, and thereby preserves the global information of the image. The segmentation task finally outputs C probability maps for C object classes (including the background), and can be trained with a pixelwise softmax loss against the ground-truth segmentation map.

3) *Saliency Detection Task*: In the saliency task, our network aims to find the interesting objects from the image. Specifically, we use one convolution layer and one deconvolution layer to generate the saliency map (normalized to $[0, 1]$ by the sigmoid function). Finally, the saliency network ends up with a squared Euclidean loss layer for saliency regression, which learns the saliency properties from data.

4) *Multi-Task Learning*: In the experiments, we perform FCNN learning by taking into account the saliency detection task in conjunction with the segmentation task. Let $\mathcal{X} = \{\mathbf{X}_i\}_{i=1}^{N_1}$ denote a collection of training images (with the width and height of each image being respectively P and Q), $\{\mathbf{Y}_{ijk} | \mathbf{Y}_{ijk} \in \{1, 2, \dots, C\}\}_{N_1 \times P \times Q}$ denote their corresponding pixelwise ground truth segmentation maps; and $\mathcal{Z} = \{\mathbf{Z}_i\}_{i=1}^{N_2}$ denote a set of training images with the corresponding ground truth saliency maps being $\{\mathbf{M}_i\}_{i=1}^{N_2}$. Furthermore, we denote all the parameters in the shared convolution part as θ_s ; the parameters in the segmentation task as θ_h ; and the parameters in the saliency task as θ_f . Our FCNN is trained by minimizing the following cost functions:

$$\begin{aligned} \mathbf{J}_1(\mathcal{X}; \theta_s, \theta_h) &= \\ &- \frac{1}{N_1} \sum_{i=1}^{N_1} \sum_{c=1}^C \sum_{j=1}^P \sum_{k=1}^Q \mathbb{1}\{\mathbf{Y}_{ijk} = c\} \log(h_{cjk}(\mathbf{X}_i; \theta_s, \theta_h)); \\ \mathbf{J}_2(\mathcal{Z}; \theta_s, \theta_f) &= \frac{1}{N_2} \sum_{i=1}^{N_2} \|\mathbf{M}_i - f(\mathbf{Z}_i; \theta_s, \theta_f)\|^2 \end{aligned} \quad (1)$$

where $\mathbb{1}$ is the indicator function; h is a semantic segmentation function returning C probabilistic segmentation maps and h_{cjk} is the (j, k) -th element of the c -th probabilistic segmentation map; and f is the saliency map output function. Clearly, the first one is associated with the cross-entropy loss term for the segmentation task, while the second cost function corresponds to the squared Euclidean loss term for the saliency task.

Subsequently, we train the network by the stochastic gradient descent (SGD) method to minimize the above cost functions with regularization on all the training samples. In practice, we carry out the segmentation task and the saliency task in an alternating manner. Namely, we first learn the parameters θ_s and θ_h for the segmentation task, and then learn the parameters θ_f as well as update the parameters θ_s for the saliency task. The above procedure is iteratively repeated as training proceeds.

We present some intuitive examples to show that our network captures the underlying saliency properties in Figure 4. Specifically, the saliency value of the red flower in Figure 4(a) is higher than the yellow one, which is consistent with human perception (paying more attention to the objects with red bright colors [15], [38]). Given an image with only the background (e.g., the lawn shown in Figure 4(b)), people often put their eyes at the center of the image [21]. As shown in Figure 4(c), our network is able to detect objects with a high contrast to the surroundings [20] (i.e., the salient orange slice is distinct from the surrounding oranges in shape and texture). With the help from the semantic segmentation learning task, our network is able to detect the semantic objects in the scene, as shown in Figure 4(d).

C. Regularized Regression for Refinement

As shown in Figure 4, the saliency maps generated from the fully convolutional neural network are usually with fuzzy object boundaries. In order to well preserve the object boundaries for the saliency maps, we make use of internally homogeneous and boundary-preserving superpixels (obtained by oversegmentation using SLIC [39]) as basic representation units, and then construct a superpixel-level adjacency graph to model the topological relationships among superpixels in both spatial and feature dimensions. More specifically, a given image is first oversegmented into a set of superpixels $\{\mathbf{x}_i\}_{i=1}^N$, each of which is represented by a Lab color vector (obtained by averaging the pixelwise color features within the superpixel).

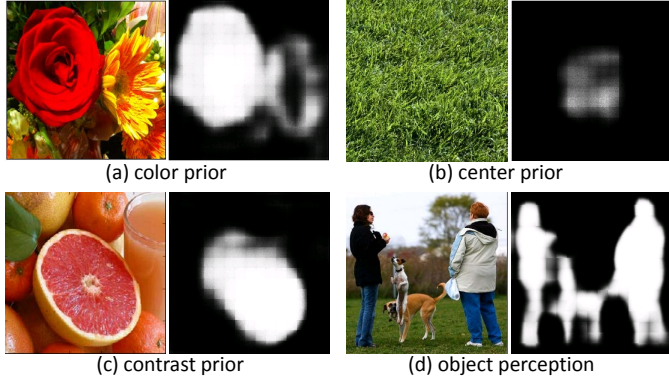


Fig. 4: Some intuitive examples of the saliency properties learned in our network, which are consistent with human perception. Given an image, people tend to pay their attention to red objects [15], [38] (a), the image center [21] (b), regions with high contrast in texture and shape [20] (c), and semantic objects [4] (d).

Therefore, the superpixel-level graph with the affinity matrix $W = (w_{ij})_{N \times N}$ is constructed as follows:

$$w_{ij} = \begin{cases} K(\mathbf{x}_i, \mathbf{x}_j) & \text{if } \mathbf{x}_i \text{ and } \mathbf{x}_j \text{ are spatially adjacent} \\ 0 & \text{Otherwise} \end{cases} \quad (2)$$

where $K(\mathbf{x}_i, \mathbf{x}_j)$ stands for the RBF kernel evaluating the feature similarity (such that $K(\mathbf{x}_i, \mathbf{x}_j) = \exp(-\frac{1}{\rho} \|\mathbf{x}_i - \mathbf{x}_j\|_2^2)$). Let $\mathbf{y} = (y_1, \dots, y_N)^\top$ denote the pre-specified saliency score vector (ranging from [-1, 1]) corresponding to the superpixels $\{\mathbf{x}_i\}_{i=1}^N$. In terms of graph-based semi-supervised regression, some superpixels are treated as seed samples with pre-specified saliency scores (such as boundary superpixels), and the saliency states for the remaining superpixels are temporarily undetermined (initialized to be 0) until they are reached by propagation. Without loss of generality, we assume the first l superpixels have the initial saliency information while the last u superpixels are null (such that $N = l + u$). Hence, our task is to learn a nonlinear regression function for saliency prediction over a given superpixel \mathbf{x} (such that $g(\mathbf{x}) = \sum_{j=1}^N \alpha_j K(\mathbf{x}, \mathbf{x}_j)$) within the following optimization framework:

$$\min_g \frac{1}{l} \sum_{i=1}^l (y_i - g(\mathbf{x}_i))^2 + \gamma_A \|g\|_K^2 + \frac{\gamma_I}{(l+u)^2} \mathbf{g}^\top \mathbf{L} \mathbf{g} \quad (3)$$

where $\|g\|_K$ denotes the norm of g in the RKHS [40] induced by the kernel function K ; $\mathbf{g} = (g(\mathbf{x}_1), \dots, g(\mathbf{x}_N))^\top$; \mathbf{L} stands for the graph Laplacian matrix for the affinity matrix W ; and γ_A as well as γ_I are two trade-off control factors ($\gamma_A = 10^{-6}$ and $\gamma_I = 1$ in the experiments). Clearly, the first term in the above optimization problem corresponds to the squared regression loss, and the third term ensures the spatial smoothness of the final saliency map. The above optimization problem can be equivalently transformed to:

$$\min_{\alpha} \frac{1}{l} \|\mathbf{y} - \mathbf{J} \mathbf{K} \alpha\|_2^2 + \gamma_A \alpha^\top \mathbf{K} \alpha + \frac{\gamma_I}{(l+u)^2} \alpha^\top \mathbf{K} \mathbf{L} \mathbf{K} \alpha \quad (4)$$

where $\mathbf{J} = \text{diag}(\underbrace{1, \dots, 1}_{l}, \underbrace{0, \dots, 0}_u)$ is a diagonal matrix, α corresponds to the nonlinear regression coefficient vector

$(\alpha_i)_{i=1}^N$, and $\mathbf{K} = (K(\mathbf{x}_i, \mathbf{x}_j))_{N \times N}$ is the kernel Gram matrix. The optimal solution to the above optimization problem is formulated as:

$$\alpha^* = \left(\mathbf{J} \mathbf{K} + \gamma_A l \mathbf{I} + \frac{\gamma_I l}{(l+u)^2} \mathbf{L} \mathbf{K} \right)^{-1} \mathbf{y} \quad (5)$$

As a result, we have the nonlinear regression function $g(\mathbf{x}) = \sum_{i=1}^N \alpha_i^* K(\mathbf{x}, \mathbf{x}_i)$ with α_i^* being the i -th element of α^* . Based on $g(\mathbf{x})$, we can compute the saliency score for any given superpixel \mathbf{x} within an image.

D. Generating Saliency Map

Given an image, the saliency map is computed in four stages: 1) object perception by FCNN; 2) image boundary information propagation within the superpixel graph; 3) coarse-grained saliency information fusion; and 4) fine-grained saliency map generation by nonlinear regression-based propagation, as illustrated in Figure 5.

For 1), the trained FCNN is used to adaptively capture the semantic structural information on object perception, resulting in a pixelwise objectness probability map (ranging from 0 and 1), which we refer as a *DeepMap*. This stage focuses on modeling the underlying object properties from the viewpoint of foreground discovery using FCNN.

In contrast, the stage 2) aims to explore the influence of the image boundary information in saliency detection from the viewpoint of background propagation. Namely, we use the learned regression function (defined in Eq. 4) based on a Laplacian graph to estimate the saliency values on the superpixel level where the ones on the image boundary are initialized -1 and others as 0. After the propagation process, we have a saliency map denoted as *BoundaryMap* (normalized to [0, 1]).

In stage 3), we perform saliency fusion of the *DeepMap* and *BoundaryMap* to generate the coarse-grained saliency map (referred to as *CgMap*) by

$$CgMap = DeepMap^{1-\beta} \circ BoundaryMap^\beta \quad (6)$$

where β is a trade-off control factor and \circ is the elementwise product operator.

In stage 4), the normalized *CgMap* (s.t. [-1, 1]) is fed into Eq. 4 for saliency refinement over the superpixel graph, resulting in the final fine-grained saliency map. As shown in Figure 5, based on graph Laplacian regularized nonlinear regression, our saliency detection approach is able to obtain more accurate saliency detection results with fine-grained object boundaries.

III. EXPERIMENTAL RESULTS

A. Experimental Setup

1) *Datasets*: In order to evaluate the performance of the proposed approach, we conduct a set of qualitative and quantitative experiments on eight benchmark datasets annotated with pixelwise ground-truth labeling, including the ASD [2], DUT-OMRON [25], ECSSD [24], PASCAL-S [41], THUR [42], THUS [23], SED2 [43], and SOD [44] datasets. Specifically,

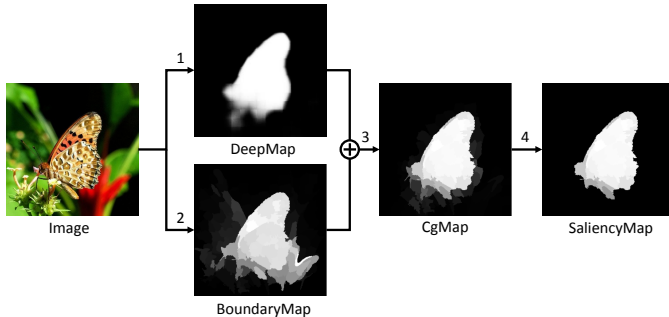


Fig. 5: Generating a saliency map with four stages. Clearly, our saliency detection approach obtains a visually precise saliency map.

the first six datasets are composed of object-centric images distributed in relatively simple scenes (e.g., high object contrast and clean background). In contrast, the last two datasets are more challenging with multiple salient objects and background clutters in images. For descriptive convenience, Table 1 shows the basic information of these eight datasets.

Dataset	ASD	THUS	THUR	DUT-OMRON	ECSSD	PASCAL-S	SOD	SED2
Size	1000	10000	6232	5168	1000	850	300	100

TABLE I: Illustration of the image numbers associated with the eight datasets.

More specifically, ASD is a commonly used dataset in salient object detection. For each image in ASD, there is usually one dominant salient object with simple backgrounds. Compared with ASD, THUS has a larger dataset size, and covers more saliency cases. It is noted that ASD is a subset of THUS. Moreover, THUR is generated by crawling from Flickr, and consists of the images with 5 object classes, including “butterfly”, “coffee mug”, “dog jump”, “giraffe”, and “plane”. Among these images, there are 6232 images that have pixelwise saliency annotation maps used for saliency detection. Aiming at overcoming the drawbacks of ASD (i.e., limited objects and simple background), DUT-OMRON is manually selected from more than 140,000 natural images, each of which has one or more salient objects and relatively complex backgrounds. As an extension of the Complex Scene Saliency Dataset(CSSD) [24], ECSSD is obtained by aggregating the images from the two publicly available datasets (i.e., BSD [45] and PASCAL VOC [46]) and the internet. PASCAL-S is generated from the PASCAL VOC dataset [46] with 20 object categories and complex scenes. SED2 is a multi-saliency-object dataset that usually includes two salient objects in each image. SOD is composed of the images (based on the BSD dataset [45]) with one or more objects and complex backgrounds. A few images in SOD are also part of ECSSD.

2) *Implementation details*: In the experiments, our algorithm is implemented in MATLAB on a desktop computer with an Intel E5-2609 CPU(2.4 GHz) and 8 GB RAM. During the saliency regression process, the superpixel oversegmentation is carried out by the SLIC method [39] with the superpixel number N being 200. The scaling factor ρ in the RBF kernel is set to 0.1.

The fully convolutional neural network (FCNN) is implemented on the basis of the Caffe [47] toolbox. More specifici-

cally, we initialize the first 13 convolutional layers of FCNN with those of the pretrained VGG 16-layer net [29] and transfer the learned representations by fine-tuning [48] to the semantic segmentation task and the saliency detection task. We construct the deconvolution layers by upsampling, whose parameters are initialized as simple bilinear interpolation parameters and iteratively updated during training. We resize all the images and ground-truth maps to 500×500 pixels for training, the momentum parameter is chosen as 0.99, the learning rate is set to 10^{-10} , and the weight decay is 0.0005. The SGD learning procedure is accelerated using a NVIDIA Tesla K40C GPU device, and takes around 3 days in 80,000 iterations.

In the experiments, the segmentation task and the saliency detection task in the FCNN are optimized in an alternating manner. Both two tasks share the parameters θ_s of the shared convolution part. Namely, we firstly perform the segmentation task using the object class segmentation dataset (i.e., PASCAL VOC 2007 with the number of object classes $C = 21$) to obtain θ_s and the segmentation-related network parameters θ_h . More specifically, the detailed training procedure is carried out as follows:

- 1) Initialize the parameters θ_s^0 of the shared fully convolutional part using the pretrained VGG 16-layer net.
- 2) Initialize the parameters θ_h^0 (for the segmentation task) and θ_f^0 (for the saliency task) randomly from the normal distribution.
- 3) Based on θ_s^0 and θ_h^0 , utilize SGD to train the segmentation-related net for updating these two parameters, resulting in θ_s^1 and θ_h^1 .
- 4) Using θ_s^1 and θ_f^0 , perform SGD to train the saliency-related net for updating the saliency-related parameters, resulting in θ_s^2 and θ_f^1 .
- 5) Based on θ_s^2 and θ_h^1 , use SGD to train the segmentation-related net for obtaining θ_s^3 and θ_h^2 .
- 6) Using θ_s^3 and θ_f^1 , perform SGD to train the saliency-related net for updating the saliency-related parameters, resulting in θ_s^4 and θ_f^2 .
- 7) Repeat the above steps (3)-(6) until obtaining the final parameters θ_s , θ_h and θ_f .

We note that the above experimental configurations are fixed throughout all the experiments.

B. Evaluation Metrics

In the experiments, we utilize four metrics for quantitative performance evaluations, including Precision and Recall (PR) curve, F-measure, mean absolute error (MAE), ROC curve and area under ROC curve (AUC). Specifically, the PR curve reflects the object retrieval performance in precision and recall by binarizing the final saliency map using different thresholds (usually ranging from 0 to 255). The F-measure characterizes the balance degree of object retrieval between precision and recall such that:

$$F_\eta = \frac{(1 + \eta^2) \text{Precision} \times \text{Recall}}{\eta^2 \times \text{Precision} + \text{Recall}} \quad (7)$$

where η^2 is typically set to 0.3 like the most existing literature work, The Precision and Recall rates correspond to the object

retrieval performance after binarization using a particular threshold.

Typically, maximum F-measure (maxF) is associated with the maximum F-measure value computed from the PR curve (as suggested in [49]), while average F-measure (aveF) uses the adaptive threshold (i.e., twice the average value of the final saliency map [2]) for binarization. In addition, MAE refers to the average pixelwise error between the saliency map and ground truth. The ROC curves are plotted w.r.t. false positive rate (FPR) and true positive rate (TPR), which are defined as follows:

$$FPR = \frac{M \cap \bar{G}}{G}, \quad TPR = \frac{M \cap G}{G} \quad (8)$$

where M denotes the binary mask of the saliency map with a particular binarization threshold, G denotes the groundtruth binary map, and \bar{G} denotes the opposite of G . In the experiments, the ROC curves are generated by varying the binarization thresholds from 0 to 255 over the final saliency maps.

Finally, AUC evaluates the object detection performance, and computes the area under the standard ROC curve (w.r.t. false positive rate and true positive rate).

C. State-of-the-art performance comparison

We qualitatively and quantitatively compare the proposed approach with several state-of-the-art methods including DRFI [33], Wco [26], IT [11], SF [50], GC [6], GMR [25], FT [2], MC [5], GB [1], HS [24], SVO [4], DSR [51], LEGS [34], BL15 [52] and BSCA [27]. Among these methods, DRFI (random forest regressor) and LEGS (deep learning) are also learning-based methods; MC and DSR (background prior), SVO (objectness + visual saliency), SF and HS (global contrast), Wco, GMR and MC (boundary prior), BL15 (center and color priors + bootstrap learning) are state-of-the-art salient object detection models which designed with different assumptions; the classic methods IT, GB and FT are included as a baseline. Most of the saliency maps associated with the competing approaches can be obtained by running their publicly available source code using the default experimental configurations. For the LEGS, BL15 and BSCA methods, we use the results reported in the literature.

1) *Quantitative performance comparison*: Figure 6 shows the corresponding PR curve performance of all the competing approaches on the eight benchmark datasets. Figure 7 shows the F-measure curves w.r.t. different binarization thresholds over the final saliency maps (i.e., 256 thresholds ranging from 0 to 255). In addition, we also show the ROC curves in Figure 8. From Figure 7 and Figure 8, we observe that the proposed approach achieves a better performance in F-measure and ROC than the other ones in most cases.

More specifically, Table II reports their quantitative saliency detection performance w.r.t. the four evaluation metrics (i.e., aveF, maxF, AUC, and MAE) on the eight benchmark datasets. From Figure 6 and Table II, it is clearly seen that our approach performs favorably against the state-of-the-art methods in most cases. On average, our approach performs better than the second best method (DRFI) by 7.22%, 7.52%, 2.54% and 21.25% in terms of aveF, maxF, AUC and MAE.

2) *Qualitative performance comparison*: For an intuitive illustration, we provide the saliency detection results of our approach over several challenging sample images against the other state-of-the-art approaches. Figure 9 shows that our approach is able to obtain favorable saliency detection results than the other methods. For example, as shown in the third and eighth rows, our approach still works well in the cases of background clutter and low foreground-background contrast.

For a more intuitive illustration of the proposed approach, Figure 10 displays the saliency detection results of the competing methods over some challenging sample images. It is clearly seen from Figure 10 that the proposed approach obtains more visually feasible saliency detection results.

D. Analysis of Proposed Approach

1) *Training strategies of FCNN*: We present the details on how to generate the training data for FCNN in our saliency detection algorithm. Here, we take three different approaches to generate training data. One is the leave-one-out strategy, the second is the baseline-reference strategy, and the third is the small-training-set strategy, which are respectively referred to as OurLO, OurBR and OurST. Specifically, as for OurLO, when we test the performance for a given dataset, the saliency training data for this dataset are derived from the images (including the annotated saliency maps) from the other datasets. As for OurBR, we just select the largest and most representative dataset (i.e., THUS) as the baseline-reference training data, and the other 7 datasets are used for testing. As for OurST, evaluate the quantitative performance of the proposed approach using a relatively small training set, which is the exactly same as that of the DRFI approach [33]. Namely, the training set is generated by selecting 2500 images from the MSRA5000 [21] (also called MSRA-B) dataset. We note that some datasets are partly overlapped with the others, e.g., ASD and THUS, ECSSD and SOD. Therefore, we make sure that the test data are disjoint from the training data (by removing the overlapping images).

The third and fourth columns of Table II show the corresponding quantitative saliency detection results of OurLO and OurBR, respectively. Clearly, such two strategies achieve comparable saliency detection results. That is, both approaches perform similarly. The performance of OurLO is slightly better than that of OurBR as more training data are used. Table III shows the quantitative results of OurLO, OurBR, OurST and DRFI on datasets which are not overlapped with the training set. We also report the results of OurST and DRFI on the MSRA5000 dataset (using the same testing list as that of DRFI with 2000 images), as shown in Figure 11. From the above results, we observe that OurST still obtains comparable results with OurLO and OurBR using more training data, and also performs better than DRFI in most cases. For consistency, our approach always refers to OurLO in the following.

2) *Evaluation on multi-task learning*: We evaluate the performance differences of the proposed approach with and without multi-task learning. Namely, the proposed approach without multi-task learning is associated with that of only using the saliency-related network, resulting in the single-task version. By taking the same baseline-reference strategy

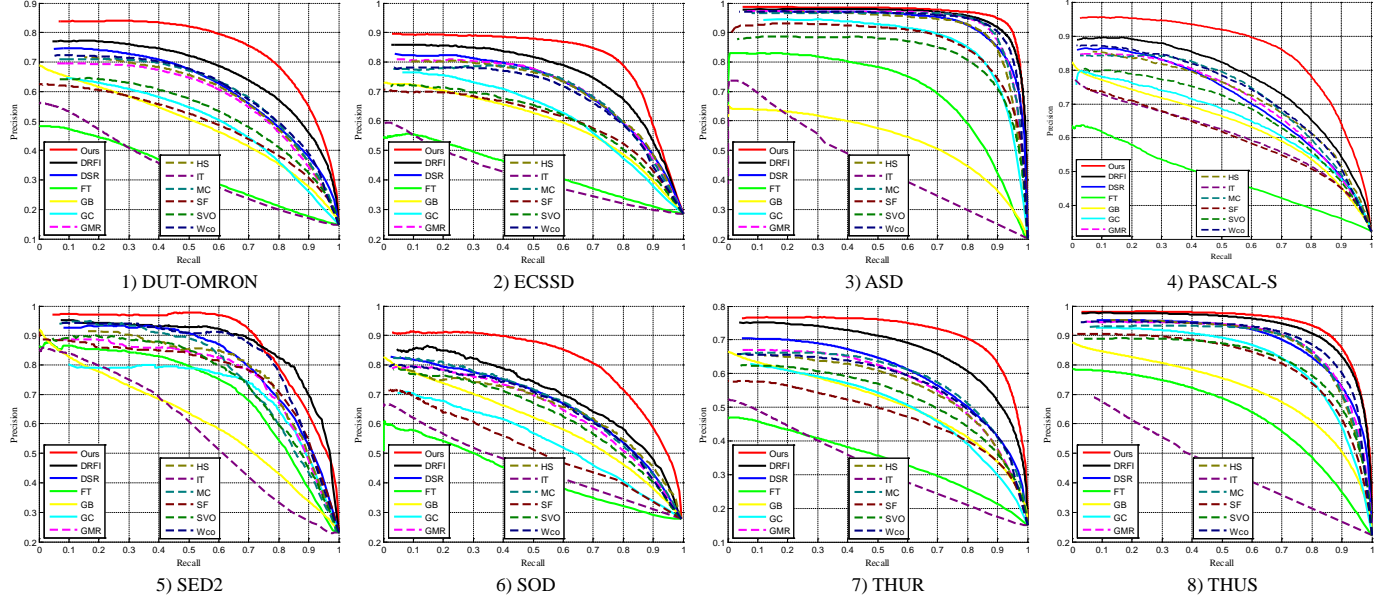


Fig. 6: Precision-recall curves of different saliency detection methods on 8 benchmark datasets. Overall, the proposed approach performs well with higher precision in the case of a fixed recall.

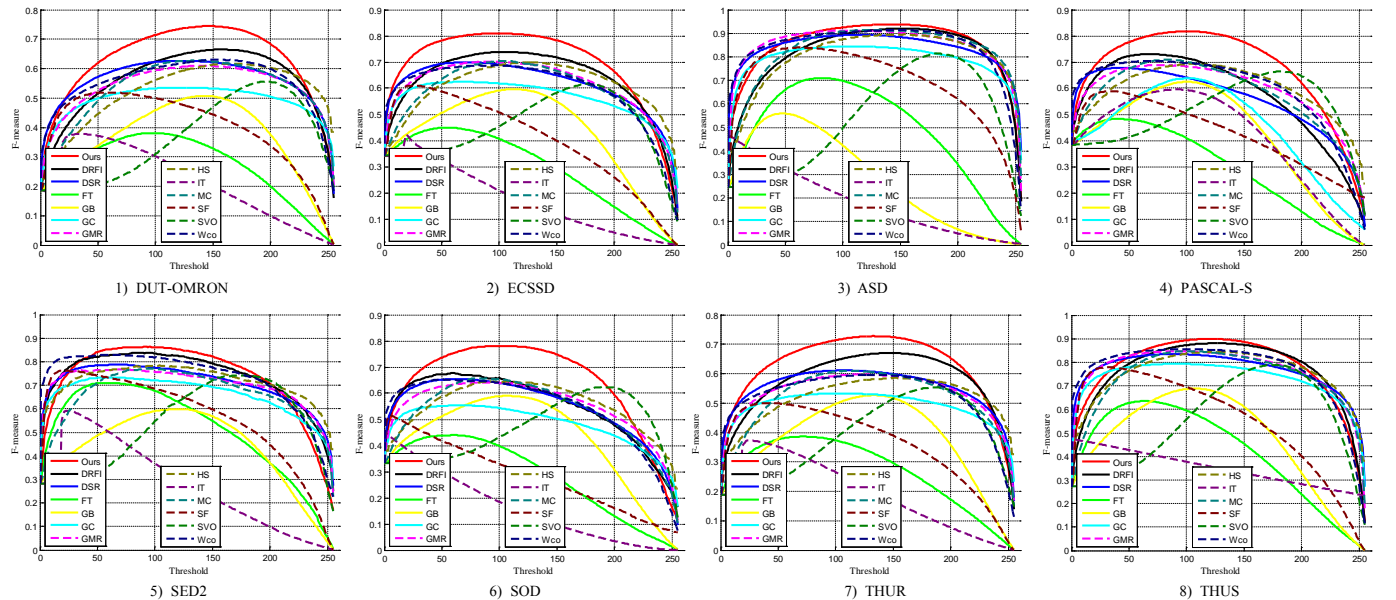


Fig. 7: F-measure curves on the eight benchmark datasets with different binarization thresholds ranging from 0 to 255. Overall, our approach achieves a higher F-measure performance than the other methods in most cases.

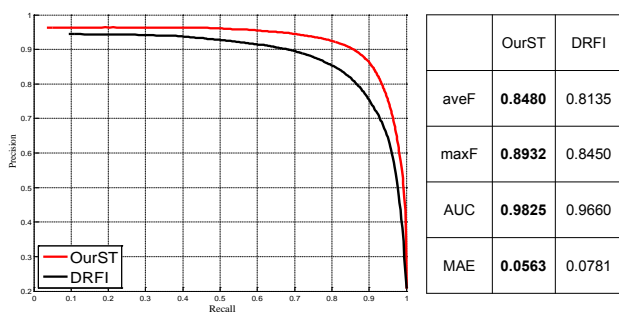


Fig. 11: Comparisons of OurST and DRFI methods on MSRA5000 dataset, including precision-recall curves and the results of four evaluation metrics.

	DUT-OMRON				ECSSD			
	aveF	maxF	AUC	MAE	aveF	maxF	AUC	MAE
OurLO	0.6045	0.7449	0.9516	0.0758	0.7589	0.8095	0.9009	0.1601
OurBR	0.5947	0.6963	0.9137	0.0963	0.7331	0.7928	0.8968	0.1602
OurST	0.5824	0.7290	0.9454	0.0828	0.7365	0.7987	0.8975	0.1602
DRFI	0.5519	0.6650	0.9335	0.0978	0.6884	0.7390	0.8770	0.1841

TABLE III: Evaluations of different approaches including OurLO, OurBR, OurST and DRFI. The method OurST uses a small training set (i.e., 2500 images from the MSRA5000 dataset). We observe that OurST still obtains comparable results with OurLO and OurBR using more training data, and also performs better than DRFI in most cases.

in the paper, we directly train the model on the THUS dataset (excluding the overlapped part). Table IV shows the comparison results on the seven datasets (except THUS).

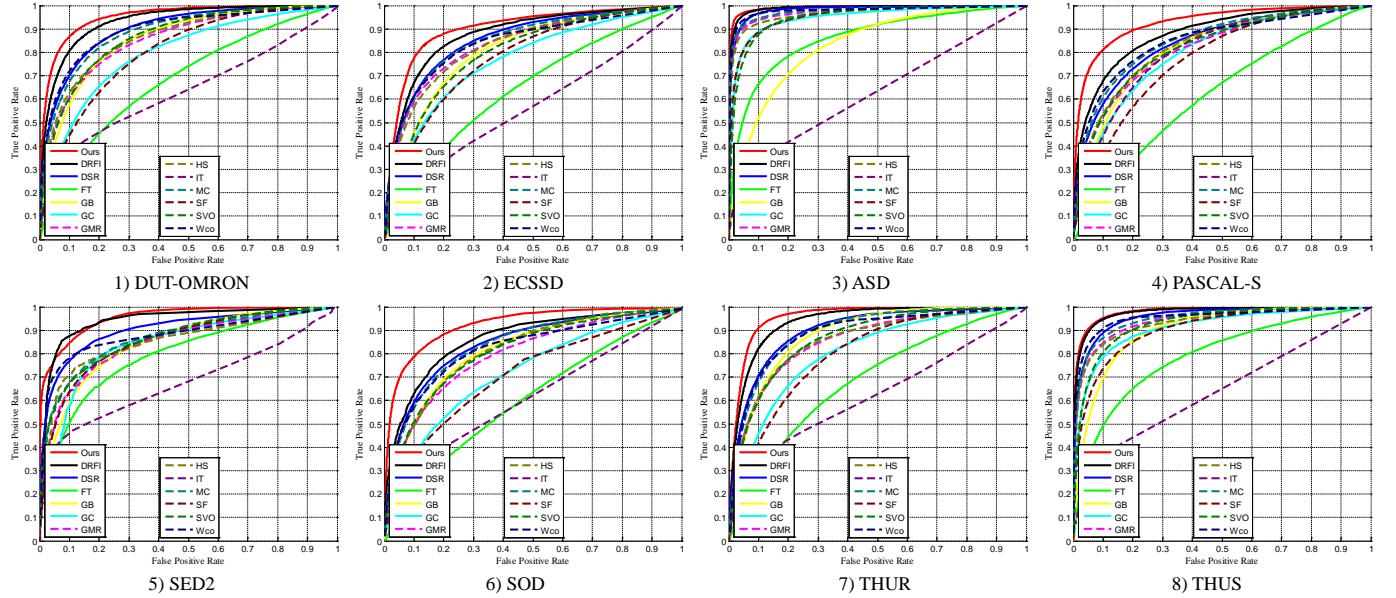


Fig. 8: ROC curves on the eight benchmark datasets. Clearly, our approach performs best in most cases.

Dataset		OurLO	OurBR	DRFI	Wco	GMR	DSR	MC	FT	GB	GC	HS	IT	SF	SVO	LEGS	BL15	BSCA
DUT-OMRON	aveF	0.6045	0.5947	0.5519	0.5276	0.5288	0.5264	0.5331	0.3122	0.4066	0.4621	0.5135	0.3179	0.4564	0.2711	-	-	-
	maxF	0.7449	0.6963	0.6650	0.6305	0.6097	0.6265	0.6274	0.3810	0.5073	0.5356	0.6162	0.3778	0.5194	0.5573	-	-	-
	AUC	0.9516	0.9137	0.9335	0.8937	0.8527	0.8990	0.8869	0.6820	0.8565	0.7956	0.8602	0.6359	0.8031	0.8656	-	-	-
	MAE	0.0758	0.0963	0.1119	0.1409	0.1113	0.1210	0.1761	0.1587	0.1675	0.1568	0.1479	0.1452	0.3116	-	-	0.196	
ECSSD	aveF	0.7589	0.7331	0.6884	0.6417	0.6498	0.6539	0.6549	0.3785	0.5205	0.5535	0.5927	0.2989	0.5229	0.1853	0.7270	-	-
	maxF	0.8095	0.7928	0.7390	0.6872	0.7012	0.6987	0.7037	0.4493	0.5966	0.6240	0.6983	0.4220	0.6104	0.6166	-	-	-
	AUC	0.9009	0.8968	0.8770	0.8398	0.8344	0.8555	0.8495	0.6443	0.8047	0.7655	0.8293	0.5655	0.7772	0.7986	-	-	-
	MAE	0.1601	0.1602	0.1841	0.2051	0.2040	0.2127	0.2055	0.2859	0.2469	0.2382	0.2064	0.2829	0.2597	0.3384	0.1910	-	0.183
ASD	aveF	0.8932	0.8881	0.8803	0.8787	0.8917	0.8589	0.8910	0.6688	0.5284	0.8196	0.8516	0.4248	0.8134	0.4141	-	-	-
	maxF	0.9380	0.9345	0.9204	0.9142	0.9114	0.8935	0.9142	0.7100	0.5591	0.8446	0.8953	0.4644	0.8392	0.8141	-	-	-
	AUC	0.9913	0.9904	0.9895	0.9786	0.9736	0.9818	0.9768	0.8619	0.8315	0.9483	0.9654	0.6300	0.9549	0.9512	-	0.9828	-
	MAE	0.0273	0.0292	0.0353	0.0400	0.0488	0.0601	0.0431	0.1466	0.1907	0.0788	0.0524	0.1959	0.1102	0.1851	-	-	0.086
PASCAL-S	aveF	0.7310	0.7300	0.6487	0.6415	0.6156	0.6172	0.6304	0.3707	0.4502	0.4151	0.5504	0.4666	0.4848	0.1713	0.6690	-	-
	maxF	0.8182	0.8051	0.7307	0.7049	0.6893	0.6782	0.7097	0.4837	0.6246	0.6384	0.6926	0.5951	0.5886	0.6639	-	-	-
	AUC	0.9287	0.9185	0.8810	0.8482	0.8143	0.8403	0.8514	0.6181	0.8166	0.7995	0.8267	0.8079	0.7696	0.8184	-	0.8682	-
	MAE	0.1695	0.1818	0.2351	0.2307	0.2464	0.2565	0.2385	0.3297	0.2703	0.2655	0.2376	0.2806	0.2983	0.3184	0.1700	-	0.225
SED2	aveF	0.7778	0.7630	0.7479	0.7776	0.7334	0.7301	0.7293	0.6324	0.4932	0.6648	0.7024	0.4762	0.7115	0.4083	-	-	-
	maxF	0.8634	0.8448	0.8386	0.8296	0.7670	0.7890	0.7710	0.7104	0.5991	0.7337	0.7837	0.5932	0.7629	0.7423	-	-	-
	AUC	0.9557	0.9447	0.9427	0.8814	0.8474	0.9052	0.8675	0.7940	0.8462	0.8354	0.8448	0.6776	0.8556	0.8666	-	0.9363	-
	MAE	0.1074	0.1142	0.1228	0.1333	0.1567	0.1452	0.1512	0.1901	0.1899	0.1800	0.1279	0.2237	0.1796	0.2094	-	-	-
SOD	aveF	0.6978	0.6910	0.6023	0.6012	0.5710	0.5980	0.5902	0.3535	0.5065	0.4632	0.5117	0.3705	0.4343	0.1540	0.6300	-	-
	maxF	0.7807	0.7659	0.6768	0.6530	0.6421	0.6543	0.6572	0.4408	0.5899	0.5551	0.6456	0.4494	0.5155	0.6242	-	-	-
	AUC	0.9233	0.9115	0.8624	0.8203	0.7950	0.8409	0.8382	0.6004	0.8143	0.7178	0.8108	0.6135	0.7077	0.8080	-	0.8477	-
	MAE	0.1503	0.1619	0.2163	0.2136	0.2303	0.2190	0.2146	0.2835	0.2360	0.2523	0.2297	0.2748	0.2663	0.3610	0.2050	-	-
THUR	aveF	0.6254	0.6116	0.5798	0.5266	0.5396	0.5422	0.5543	0.3389	0.4485	0.4732	0.5091	0.3109	0.4494	0.3175	-	-	-
	maxF	0.7276	0.7173	0.6702	0.5962	0.5972	0.6107	0.6096	0.3861	0.5265	0.5331	0.5852	0.3729	0.4998	0.5537	-	-	-
	AUC	0.9567	0.9541	0.9379	0.8865	0.8556	0.9020	0.8950	0.6837	0.8821	0.8027	0.8535	0.6232	0.7995	0.8655	-	-	-
	MAE	0.0854	0.0897	0.1050	0.1239	0.1421	0.1190	0.1254	0.1775	0.1535	0.1691	0.1582	0.1505	0.1535	0.2737	-	-	-
THUS	aveF	0.8630	-	0.8514	0.8357	0.8322	0.8095	0.8338	0.5933	0.6409	0.7648	0.8006	0.4334	0.7433	0.4185	-	-	-
	maxF	0.8994	-	0.8807	0.8559	0.8469	0.8346	0.8476	0.6353	0.6882	0.7938	0.8449	0.4716	0.7790	0.7895	-	-	-
	AUC	0.9810	-	0.9776	0.9547	0.9435	0.9588	0.9507	0.7896	0.9020	0.9116	0.9325	0.6404	0.9051	0.9299	-	0.9635	-
	MAE	0.0628	-	0.0684	0.0845	0.0963	0.1052	0.0932	0.1925	0.1594	0.1185	0.0920	0.2122	0.1613	0.1831	-	-	0.125

TABLE II: Comparison of average F-measure using adaptive threshold (aveF), maximum F-measure of average precision recall curve (maxF), AUC scores and MAE scores (smaller better). Our approach (OurLO) achieves the best performance in all these metrics. The results from the last two columns are directly quoted from their original papers. Since using THUS for training, the saliency results of OurBR are null.

Clearly, multi-task learning helps to learn a better model for saliency detection in most cases.

3) *Evaluation on regression-based propagation:* We quantitatively compare our approach with and without nonlinear regression-based propagation on the eight benchmark datasets. Table V shows that our approach with propagation will lead to a better saliency detection performance in most cases compared with that without propagation. The underlying reason can be attributed to that nonlinear regression-based propagation can capture more topological information (among

superpixels) that is helpful to the boundary preservation of salient objects.

4) *Effect of β :* To analyze the relative effect of nonlinear saliency regression using deep saliency learning and image boundary propagation, we perform quantitative experiments (on the ASD dataset) to evaluate the saliency detection performance w.r.t. different configurations of the trade-off control factors β such that $\beta \in \{0.0, 0.1, 0.2, 0.3, 0.5\}$, as shown in Table VI. The results show that the setting of $\beta = 0.2$ leads to a better performance in most cases. Moreover, the performance

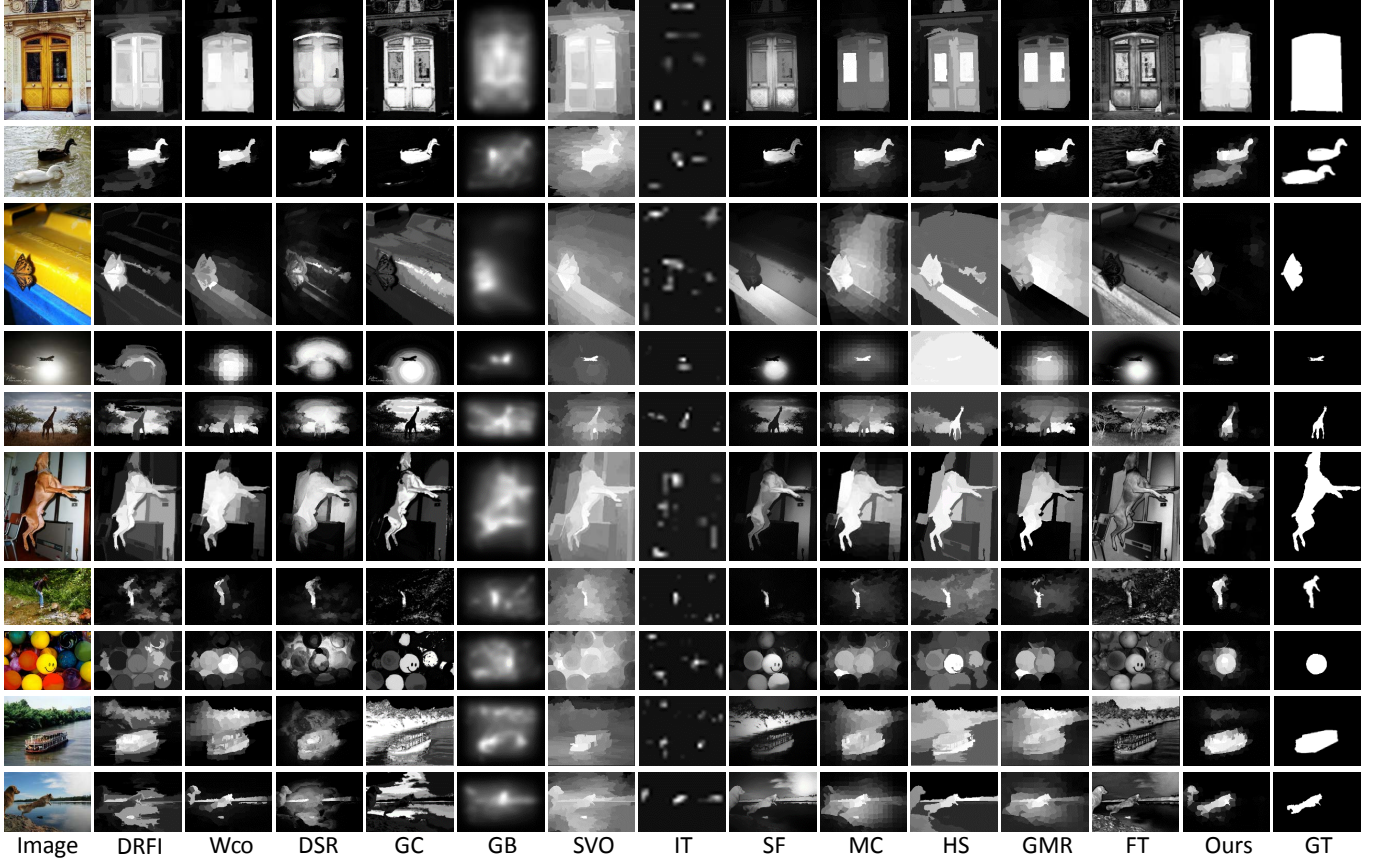


Fig. 9: Qualitative comparison of different approaches on several challenging samples with ground truth (GT). Clearly, our approach obtains more visually feasible saliency detection results than the comparison approaches.

	method	aveF	maxF	AUC	MAE
DUT-OMRON	Multi-task	0.5947	0.6963	0.9137	0.0963
	Single-task	0.5171	0.6625	0.9147	0.1155
ECSSD	Multi-task	0.7331	0.7928	0.8968	0.1602
	Single-task	0.7214	0.7852	0.8914	0.1651
ASD	Multi-task	0.8881	0.9345	0.9904	0.0292
	Single-task	0.8695	0.9201	0.9877	0.0367
PASCAL-S	Multi-task	0.7300	0.8051	0.9185	0.1818
	Single-task	0.7120	0.7995	0.9178	0.1802
SED2	Multi-task	0.7630	0.8448	0.9447	0.1142
	Single-task	0.7304	0.8272	0.9351	0.1240
SOD	Multi-task	0.6910	0.7659	0.9115	0.1619
	Single-task	0.6726	0.7607	0.9127	0.1623
THUR	Multi-task	0.6116	0.7173	0.9541	0.0897
	Single-task	0.5998	0.7163	0.9528	0.0898
Average		0.7159	0.7938	0.9328	0.1190
Single-task		0.6890	0.7816	0.9303	0.1248

TABLE IV: Comparison of the proposed approach with (Multi-task, same as OurBR) and without multi-task learning on the seven datasets (except THUS). Clearly, our approach with multi-task learning achieves a better performance in most cases.

of our approach keeps relatively stable w.r.t. different choices of β . When $\beta = 0$, only the saliency information from FCNN is used. With the increase of β , our saliency performance gradually improves until $\beta = 0.2$. After that, the performance keeps relatively stable. Therefore, our deep saliency learning part plays a crucial role in capturing the semantic object properties, while image boundary propagation can result in a slight improvement due to introducing more spatial structural information. The trade-off control factors β for coarse-grained saliency fusion is set to 0.2 in all the experiments.

	method	aveF	maxF	AUC	MAE
DUT-OMRON	with Pro	0.6045	0.7449	0.9516	0.0758
	w/o Pro	0.5970	0.7155	0.9502	0.0833
ECSSD	with Pro	0.7589	0.8095	0.9009	0.1601
	w/o Pro	0.7245	0.8031	0.8905	0.1463
ASD	with Pro	0.8932	0.9380	0.9913	0.0273
	w/o Pro	0.8500	0.9055	0.9883	0.0407
PASCAL-S	with Pro	0.7310	0.8182	0.9287	0.1695
	w/o Pro	0.6266	0.8087	0.9191	0.1499
SED2	with Pro	0.7778	0.8634	0.9557	0.1074
	w/o Pro	0.7502	0.8431	0.9630	0.0965
SOD	with Pro	0.6978	0.7807	0.9233	0.1503
	w/o Pro	0.6711	0.7774	0.9239	0.1280
THUR	with Pro	0.6254	0.7276	0.9567	0.0854
	w/o Pro	0.6209	0.7309	0.9561	0.0908
THUS	with Pro	0.8630	0.8994	0.9810	0.0628
	w/o Pro	0.7511	0.8336	0.9630	0.0973
Average		with Pro	0.7439	0.8227	0.9487
Single-task		0.6989	0.8022	0.9443	0.1041

TABLE V: Comparison of our approach with (with Pro) and without (w/o Pro) non-linear regression-based propagation. In most cases, our approach with propagation achieves a better performance.

IV. CONCLUSION

In this paper, we propose a simple yet effective multi-task deep saliency approach for salient object detection based on the fully convolutional neural network with global input (whole raw images) and global output (whole saliency maps). The proposed saliency approach models the intrinsic

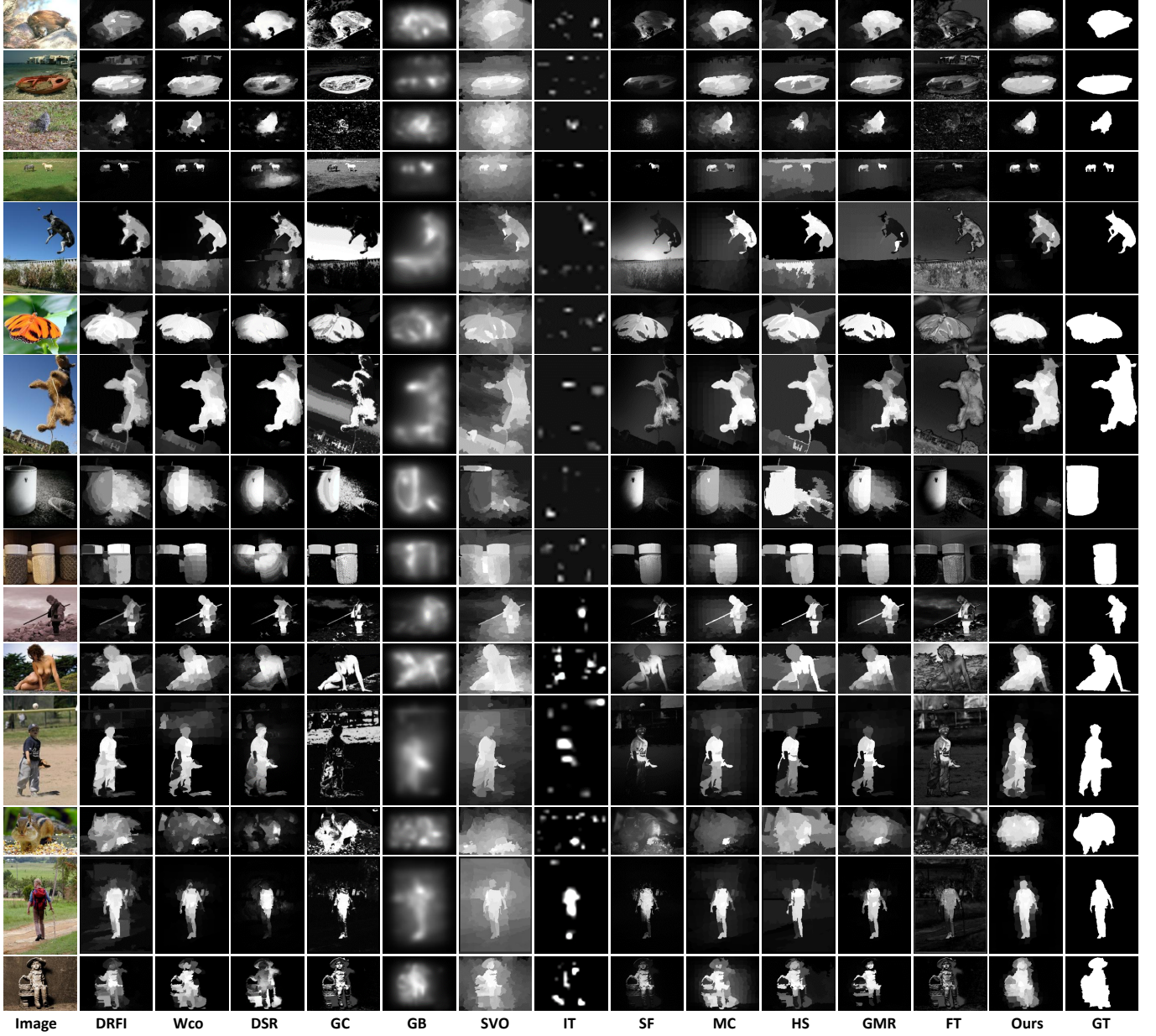


Fig. 10: Saliency detection results of all the comparison approaches over several challenging sample images. Clearly, our approach obtains more visual feasible saliency detection results.

	0	0.1	0.2	0.3	0.5
aveF	0.8689	0.8783	0.8932	0.9043	0.9143
maxF	0.9195	0.9352	0.9380	0.9368	0.9318
AUC	0.9880	0.9910	0.9913	0.9910	0.9895
MAE	0.0329	0.0284	0.0273	0.0304	0.0431

TABLE VI: Evaluation of our saliency detection approach using different value of β . The columns (from left to right) show the quantitative results on the ASD datasets when β are chosen from $\{0, 0.1, 0.2, 0.3, 0.5\}$. Clearly, the performance of our approach is relatively stable w.r.t. different choices of β , and we choose $\beta = 0.2$ in our experiments.

semantic properties of salient objects in a totally data-driven manner, and performs collaborative feature learning for the two correlated tasks (i.e., saliency detection and semantic image segmentation), which generally leads to the saliency

performance improvement in object perception. Moreover, it is capable of accomplishing the feature-sharing task by using a sequence of fully convolutional layers, resulting in a significant reduction of feature redundancy. In order to obtain more fine-grained saliency detection results, we present a superpixel-driven saliency refinement model based on graph Laplacian regularized nonlinear regression with a closed-form solution, which aims to propagate the saliency information over the spatially-adjacent superpixel graph for further saliency performance enhancement. Experimental results on the eight benchmark datasets demonstrate the proposed approach performs favorably in different evaluation metrics against the state-of-the-art methods.

REFERENCES

- [1] J. Harel, C. Koch, and P. Perona, "Graph-based visual saliency," in *NIPS*, 2006.
- [2] R. Achanta, S. Hemami, F. Estrada, and S. Sussstrunk, "Frequency-tuned salient region detection," in *CVPR*, 2009.
- [3] R. Valenti, N. Sebe, and T. Gevers, "Image saliency by isocentric curvedness and color," in *ICCV*, 2009.
- [4] K.-Y. Chang, T.-L. Liu, H.-T. Chen, and S.-H. Lai, "Fusing generic objectness and visual saliency for salient object detection," in *ICCV*, 2011.
- [5] B. Jiang, L. Zhang, H. Lu, C. Yang, and M.-H. Yang, "Saliency detection via absorbing markov chain," in *ICCV*, 2013.
- [6] M.-M. Cheng, J. Warrell, W.-Y. Lin, S. Zheng, V. Vineet, and N. Crook, "Efficient salient region detection with soft image abstraction," in *ICCV*, 2013.
- [7] Y. Xie, H. Lu, and M.-H. Yang, "Bayesian saliency via low and mid level cues," *IEEE Trans. Image Process.*, vol. 22, no. 5, pp. 1689–1698, 2013.
- [8] J. Sun, H. Lu, and X. Liu, "Saliency region detection based on markov absorption probabilities," *IEEE Trans. Image Process.*, vol. 24, no. 5, pp. 1639–1649, 2015.
- [9] W. Zou, Z. Liu, K. Kpalma, J. Ronsin, Y. Zhao, and N. Komodakis, "Unsupervised joint salient region detection and object segmentation," *IEEE Trans. Image Process.*, vol. 24, no. 11, pp. 3858–3873, 2015.
- [10] A. Borji, "What is a salient object? a dataset and a baseline model for salient object detection," *IEEE Trans. Image Process.*, vol. 24, no. 2, pp. 742–756, 2015.
- [11] L. Itti, C. Koch, and E. Niebur, "A model of saliency-based visual attention for rapid scene analysis," *IEEE Trans. Pattern Anal. Mach. Intell.*, vol. 20, no. 11, pp. 1254–1259, 1998.
- [12] S. Frintrop, T. Werner, and M. Garec, "Traditional Saliency Reloaded : A Good Old Model in New Shape," in *CVPR*, 2015.
- [13] H. Jiang, J. Wang, Z. Yuan, T. Liu, N. Zheng, and S. Li, "Automatic salient object segmentation based on context and shape prior," in *BMVC*, 2011.
- [14] Y. Wei, F. Wen, W. Zhu, and J. Sun, "Geodesic saliency using background priors," in *ECCV*, 2012.
- [15] X. Shen and Y. Wu, "A unified approach to salient object detection via low rank matrix recovery," in *CVPR*, 2012.
- [16] G. Li and Y. Yu, "Visual saliency based on multiscale deep features," in *CVPR*, 2015.
- [17] C. Li, Y. Yuan, W. Cai, Y. Xia, and D. D. Feng, "Robust Saliency Detection via Regularized Random Walks Ranking," in *CVPR*, 2015.
- [18] C. Gong, D. Tao, W. Liu, S. J. Maybank, M. Fang, K. Fu, and J. Yang, "Saliency Propagation from Simple to Difficult," in *CVPR*, 2015.
- [19] Y.-F. Ma and H.-J. Zhang, "Contrast-based image attention analysis by using fuzzy growing," in *ACM Multimedia*, 2003.
- [20] D. Klein and S. Frintrop, "Center-surround divergence of feature statistics for salient object detection," in *ICCV*, 2011.
- [21] T. Liu, Z. Yuan, J. Sun, J. Wang, N. Zheng, X. Tang, and H.-Y. Shum, "Learning to detect a salient object," *IEEE Trans. Pattern Anal. Mach. Intell.*, vol. 33, no. 2, pp. 353–367, 2011.
- [22] X. Li, Y. Li, C. Shen, A. Dick, and A. van den Hengel, "Contextual hypergraph modeling for salient object detection," in *ICCV*, 2013.
- [23] M.-M. Cheng, N. J. Mitra, X. Huang, P. H. S. Torr, and S.-M. Hu, "Global contrast based salient region detection," *IEEE Trans. Pattern Anal. Mach. Intell.*, vol. 37, no. 3, pp. 569–582, 2015.
- [24] Q. Yan, L. Xu, J. Shi, and J. Jia, "Hierarchical saliency detection," in *CVPR*, 2013.
- [25] C. Yang, L. Zhang, H. Lu, X. Ruan, and M.-H. Yang, "Saliency detection via graph-based manifold ranking," in *CVPR*, 2013.
- [26] W. Zhu, S. Liang, Y. Wei, and J. Sun, "Saliency optimization from robust background detection," in *CVPR*, 2014.
- [27] Y. Qin, H. Lu, Y. Xu, and HeWang, "Saliency detection via cellular automata," in *CVPR*, 2015.
- [28] A. Krizhevsky, I. Sutskever, and G. E. Hinton, "Imagenet classification with deep convolutional neural networks," in *NIPS*, 2012.
- [29] K. Simonyan and A. Zisserman, "Very deep convolutional networks for large-scale image recognition," *CoRR*, vol. abs/1409.1556, 2014.
- [30] C. Szegedy, W. Liu, Y. Jia, P. Sermanet, S. Reed, D. Anguelov, D. Erhan, V. Vanhoucke, and A. Rabinovich, "Going deeper with convolutions," *CoRR*, vol. abs/1409.4842, 2014.
- [31] P. Pinheiro and R. Collobert, "Recurrent convolutional neural networks for scene labeling," in *ICML*, 2014.
- [32] J. Long, E. Shelhamer, and T. Darrell, "Fully convolutional networks for semantic segmentation," in *CVPR*, 2015.
- [33] H. Jiang, J. Wang, Z. Yuan, Y. Wu, N. Zheng, and S. Li, "Saliency object detection: A discriminative regional feature integration approach," in *CVPR*, 2013.
- [34] L. Wang, H. Lu, and M. hsuan Yang, "Deep networks for saliency detection via local estimation and global search," in *CVPR*, 2015.
- [35] R. Zhao, H. Li, and X. Wang, "Saliency Detection by Multi-Context Deep Learning," in *CVPR*, 2015.
- [36] V. Nair and G. E. Hinton, "Rectified linear units improve restricted boltzmann machines," in *ICML*, 2010.
- [37] O. Russakovsky, J. Deng, H. Su, J. Krause, S. Satheesh, S. Ma, Z. Huang, A. Karpathy, A. Khosla, M. S. Bernstein, A. C. Berg, and L. Fei-Fei, "Imagenet large scale visual recognition challenge," *CoRR*, vol. abs/1409.0575, 2014.
- [38] L. Itti and C. Koch, "Computational modelling of visual attention," *Nature Reviews Neuroscience*, vol. 2, no. 3, pp. 194–203, 2001.
- [39] R. Achanta, A. Shaji, K. Smith, A. Lucchi, P. Fua, and S. Sussstrunk, "Slic superpixels compared to state-of-the-art superpixel methods," *IEEE Trans. Pattern Anal. Mach. Intell.*, vol. 34, no. 11, pp. 2274–2282, 2012.
- [40] M. Belkin, P. Niyogi, and V. Sindhwani, "Manifold regularization: A geometric framework for learning from labeled and unlabeled examples," *JMLR*, vol. 7, pp. 2399–2434, 2006.
- [41] Y. Li, X. Hou, C. Koch, J. M. Rehg, and A. L. Yuille, "The secrets of salient object segmentation," in *CVPR*, 2014.
- [42] M.-M. Cheng, N. J. Mitra, X. Huang, and S.-M. Hu, "Saliencyshape: Group saliency in image collections," *The Visual Computer*, vol. 30, no. 4, pp. 443–453, 2014.
- [43] S. Alpert, M. Galun, R. Basri, and A. Brandt, "Image segmentation by probabilistic bottom-up aggregation and cue integration," in *CVPR*, 2007.
- [44] V. Movahedi and J. H. Elder, "Design and perceptual validation of performance measures for salient object segmentation," in *CVPR*, 2010.
- [45] D. R. Martin, C. C. Fowlkes, and J. Malik, "Learning to detect natural image boundaries using local brightness, color, and texture cues," *IEEE Trans. Pattern Anal. Mach. Intell.*, vol. 26, no. 5, pp. 530–549, 2004.
- [46] M. Everingham, L. Van Gool, C. K. Williams, J. Winn, and A. Zisserman, "The pascal visual object classes (voc) challenge," *IJCV*, vol. 88, no. 2, pp. 303–338, 2010.
- [47] Y. Jia, E. Shelhamer, J. Donahue, S. Karayev, J. Long, R. B. Girshick, S. Guadarrama, and T. Darrell, "Caffe: Convolutional architecture for fast feature embedding," *CoRR*, vol. abs/1408.5093, 2014.
- [48] J. Donahue, Y. Jia, O. Vinyals, J. Hoffman, N. Zhang, E. Tzeng, and T. Darrell, "Decaf: A deep convolutional activation feature for generic visual recognition," in *ICML*, 2014.
- [49] D. Martin, C. Fowlkes, and J. Malik, "Learning to detect natural image boundaries using local brightness, color, and texture cues," *IEEE Trans. Pattern Anal. Mach. Intell.*, vol. 26, no. 5, pp. 530–549, 2004.
- [50] F. Perazzi, P. Krahenbuhl, Y. Pritch, and A. Hornung, "Saliency filters: Contrast based filtering for salient region detection," in *CVPR*, 2012.
- [51] X. Li, H. Lu, L. Zhang, X. Ruan, and M.-H. Yang, "Saliency detection via dense and sparse reconstruction," in *ICCV*, 2013.
- [52] N. Tong, H. Lu, and M. hsuan Yang, "Saliency object detection via bootstrap learning," in *CVPR*, 2015.